Experimental Techniques
https://doi.org/10.1007/s40799-022-00611-3

RESEARCH PAPER

Snappy: A New Automated Testing Machine for Monitoring the Break Evolution Process during Single Fiber Fragmentation Test

L. A. Ahure Powell[1] · R. J. Sheridan[2] · S. Yucel[3] · B. Yucel[3] · E. Rust[1] · S. R. Kalidindi[3] · J. Woodcock[1] · J. W. Gilman[1] · G. A. Holmes[1]

Received: 24 June 2022 / Accepted: 14 September 2022

Abstract
A measurement of interfacial shear strength (IFSS) in fiber reinforced polymer (FRP) materials remains elusive after more than fifty years. This is due in part to the many sources of uncertainty, the time-consuming nature of the measurements, and the large amount of data required to statistically overcome that variability. A new device, called Snappy, was designed to improve upon previous attempts at automating the single fiber fragmentation test (SFFT) by increasing the image acquisition rate during traditional step-strain experiment. This enhancement allows for the investigation of the fiber break evolution during matrix relaxation periods and generates a record of the time, position, and local strain of each fragmentation event. Minimizing manpower is a key motivation for designing and building this new automated apparatus. A computer program was developed to process large image data sets acquired during SFFT and to automatically locate fiber fractures and store the processed information in a database. The automated fiber detection algorithm implemented in Snappy allows for the rapid acquisition of a record of the location of each break and the stress at which that failure occurred (tier 1 data), which is important for calculating the strength of the fiber at the critical length.

Keywords Polymers · Fiber/matrix bond · Fragmentation · Interfacial strength · Stress relaxation

Introduction and Background

The urgent need to repair and modernize the Nation's civil infrastructure network and the projected price tag using traditional twentieth century solutions have spurred renewed interest in the United States Congress to encourage the use of innovative corrosion resistant materials, such as fiber reinforced plastics (FRPs) [1]. The Federal testing standards for civil infrastructure must address the challenges associated with using FRP composites in structural applications, with particular emphasis on the tremendous range of loading conditions they must withstand [2, 3]. However, for civil infrastructure, the stress-response and failure behavior of these time dependent materials can be altered by their long-term exposure to moisture, which causes plasticization of the polymer matrix, degradation, and physical aging. In addition, with the added effects of thermocycling, this can present unique challenges in predicting the fatigue and failure behavior of FRP composites.

Recognizing that the failure behavior and efficient use of FRPs must be understood at the micromechanics level, the single fiber fragmentation test (SFFT), although not accepted as a standardized test [4–6], is widely used by researchers and industry as the micromechanics test that best mimics the fiber loading behavior observed in full-scale composites. Research at the National Institute of Standards and Technology (NIST) focuses on overcoming many of the disadvantages listed in reference [6] that have impeded the development of a standardized SFFT (e.g., the manual testing of the specimen requires 6 h per test and at least 15 to 20 samples to get a statistical average, which then takes several weeks to complete for a single evaluation and data analysis) and an algorithm to automatically extract and process the tier 1 data that is essential for obtaining realistic values of the interfacial shear strength (IFSS).

✉ G. A. Holmes
gale.holmes@nist.gov

[1] Materials Science and Engineering Division, National Institute of Standards and Technology, Gaithersburg, MD, USA

[2] Department of Mechanical Engineering & Materials Science, Duke University, Durham, NC, USA

[3] Woodruff School of Mechanical Engineering, Georgia Institute of Technology, Atlanta, GA, USA

Published online: 14 October 2022

Curtin [7] observed that the SFFT method developed by DiBenedetto-Drzal [8, 9] admits the acquisition of several types of raw data for IFSS analysis: (i) a record of the location of each break and the stress at which that failure occurred (tier 1 data), (ii) reformulation of the tier 1 data at various stress or strain increments into a fiber fragment distribution (tier 2 data) where a fragment is the region of intact fiber between two neighboring breaks, and (iii) a record of the number of breaks that have occurred as a function of stress or strain (tier 3 data). It was also noted that the tier 1 raw data contains a wealth of information on the in-situ fiber strength at small gauge lengths on the order of l_c, the critical length, which is essential for obtaining an accurate estimate of the IFSS. However, there has been some debate about how to best analyze the tier 1 SFFT data to extract values for $\sigma_f\{l_c\}$ [10], which is the strength of the fiber at the critical length.

Early attempts to monitor the evolution of the fiber fracture process in the SFFT and determine $\sigma_f\{l_c\}$ focused on using the acoustic emission (AE) source location technique to obtain fiber break location data (tier 1 data), to measure actual fragment length distributions (tier 2 data), and to count the number of fiber breaks with increasing strain (tier 3 data) [11–17]. Although the AE approach as applied to the SFFT has the advantage of monitoring the fiber fracture evolution process in non-transparent matrices, Manor and Clough [18] found that the AE source location accuracy for fiber breaks in a SiC/Al test specimen is about ± 150 µm, while Rouby and Farve [19] obtained an accuracy of about ± 500 µm for fiber breaks in single fiber graphite/epoxy samples. Subsequent research by Clough and McDonough [20] noted that the AE source location technique requires complex and expensive equipment to measure the microsecond differences in arrival time, which can be defeated since the accuracy depends critically on the wave speed of the matrix. Research by Netravali et al. [11] noted that for polymer composites, the wave speed of the matrix can easily vary by 10% with the applied strain, resulting in corresponding uncertainties in the fiber break location. Additional research by Kim et al. [21] on glass fiber epoxy test specimens indicates that a break location accuracy must be much less than ± 150 µm to accurately estimate the strength of the fiber at l_c since the average fragment length ($\overline{l_f}$) at saturation can be less than ± 400 µm.

Noting these difficulties, Clough and McDonough advocated the acquisition of tier 3 data (i.e., number of fiber breaks as a function of stress or strain) as the most practical approach for determining IFSS values from the SFFT. Thus, NIST had the first-generation automatic fiber fragmentation test machine built to acquire tier 3 data by taking an image after the dwell time following each step-strain [5]; however, the automated image analysis software to detect fiber breaks was never developed [22]. Thus, all data analysis was performed manually. To address the objections of Li et al. [23], Holmes et al. acquired tier 1 data on combinatorial multi-fiber test specimens that contained a closely spaced multi-fiber array (inter-fiber spacing ≈ 1 fiber diameter) and two single fibers [21, 24]. However, due to camera limitations, the fiber break data from the first-generation automated fragmentation test machine is interval censored (i.e., when multiple fiber breaks occur within each strain-step, the fiber breaks evolution process cannot be discerned from a single camera scan at the end of the 10-min dwell time).

In this work, a new automatic system, named Snappy, was designed, built and tested to improve on the original automated test machine and overcome the many disadvantages of performing this test that were summarized after the second round-robin by Hunston et al. [5] and illustrated in Lodeiro's first table [6]. Based on data obtained from the original automated fragmentation testing system [25], it was also shown that the fragmentation process generally occurs when the matrix is exhibiting nonlinear viscoelastic behavior. Therefore, the new instrument also monitors and records the load during the step-strain process. To overcome the interval censoring that occurred in the original instrument, image acquisition in the Snappy instrument is accelerated and allows data acquisition to occur within the 10-min dwell time, thereby, providing a more complete picture of the fiber break evolution process during the early stages of the test. To handle this increased volume of data, a computer algorithm was developed to automatically catalogue the location of each fiber break. In addition, the time that the image is taken is documented, so that the stress and strain can be extracted from the load-time curve of the SFFT and facilitate the development of more accurate shear-lag models. This algorithm has proven to significantly reduce the user presence during SFFT and to quickly process very large amounts of acquired tier 1 data. This, together with rapid image acquisition, enables the automatic, repeatable generation and processing of tier 1 data to enable the accurate and precise determination of IFSS values.

Materials and Specimen Preparation

Diglycidyl ether of bisphenol-A (DGEBA, Epon 828, Miller-Stephenson), 1,4-butanedioldiglycidyl ether (DGEBD, technical grade, 60 % purity, Sigma Aldrich), and meta-phenylenediamine (m- PDA, 99 % purity, Sigma Aldrich) were used as received. A tow of E-glass fibers, functionalized with Silquest A-1100 silane coupling agent, were obtained from Owens Corning. RTV 664 (two-part silicone resin, Momentive) was used to make the silicone molds for the dogbone specimens.

The silicone molds were prepared by blending the RTV 664 (91 g part A, 9 g part B) using a high-rate (FlackTek)

speed mixer at 262 rad/s for 10 min. The mixture was poured into an eight-cavity dogbone shaped aluminum master mold (horizontally leveled and polished to a mirror finish) and cured at room temperature for 24 h. Each cavity was designed with a sprue slot at each end of the dogbone grip with raised floors to ensure fibers were placed approximately 750 µm above the surface of the silicone mold floor. After curing, the silicone molds were removed from the aluminum master and post-cured in an oven for 1 h at 150 °C then rinsed with acetone prior to use.

Approximately 30.5 cm long A-1100 E-glass fibers were extracted from the tow and held with clean gloved hands at the extremities. Single filaments were laid in each cavity sprue slot using a method previously described in [22, 26, 27]. Each fiber, with a 15 µm average diameter, was then glued in place with a Double Bubble two-part, 5-min epoxy. This was to ensure that the fiber would be held in static tension in the silicone mold during the epoxy curing step.

An epoxy blend was prepared by mixing DGEBA (80 mass %) with DGEBD (20 mass %). A stochiometric amount of m-PDA was added to the blend and degassed under a 30-mmHg vacuum for 10 min at 60 °C. The degassed mixture was then poured into the preheated molds (at 60 °C) with the pre-stressed E-glass fibers. The filled molds were then cured using the following cure schedule: (a) 22 °C to 60 °C in 14 min, (b) 60 °C hold for 3 h, (c) 60 °C to 121 °C in 22 min, (d) 121 °C hold for 2 h, (e) 121 °C to 130 °C in 3 min, and (f) 130 °C hold for 1 h [21, 28–30].

This resin system satisfies the fourth bullet point in the "disadvantages" section in Lodeiro's first table [6] about limited material applicability (or Table S1 in the supplementary material or S.M.). Each specimen was trimmed with wet sandpaper (gradually increasing the grit from 320 to 1200) to remove the excess cured materials from the edges. Both surfaces of the specimen appear optically transparent due to the mirror finish of the polished master mold. On the surface of the specimen, optically visible fiducial marks are made with a permanent marker and used to calculate the strain in the specimen matrix.

Design

Sensor and Optics

Snappy is designed to rapidly, stably, and repeatably acquire images of the entire embedded single fiber gauge length with submicron resolution. Therefore, the sensor, optical and lighting elements will be initially described. As noted as (A) in Table 1, the sensor is a line scan camera, which captures a pair of sensor lines that are 2048 pixels x 2 pixels in resolution at a maximum of 50 kHz and 12 bits per pixel, or 1.2 GB/s, with a pixel size of 10.56 µm × 10.56 µm. The camera is also equipped with a time-delay integration (TDI) mode that is used to sum the pair of sensor lines together (also known as stitching) to boost light capture and signal-to-noise and create a complete 2D image. The optical element (B) is a 10X compact adjustable objective with a 0.17 numerical aperture mounted to the camera with a 67 mm extension tube to produce a magnification of 21.17X that targets a nominal pixel size of 500 nm in both the horizontal and vertical directions. Illumination is provided by a light-emitting diode (LED) source (C), and a 2.54 cm light line with a focusing lens for uniform brightness across the entire area of the specimen. The light source is primarily operated with power to only the red LEDs to minimize photochemical damage, heating, nonuniform attenuation and scattering across wavelengths.

The sample is loaded in tension, and a nominal displacement step of 0.086 mm is applied and held for

Table 1 Notation of instruments and function (with wiring diagrams illustrated in the S.M in Fig. S2 and Fig. S3)

Notation	Instrument Name	Function
(A)	Piranha4 with Teledyne Dalsa	Line scan camera with a line rate up to 50 kHz
(B)	Edmunds Optics	10X compact adjustable objective
(C)	Schott ColdVision- Light Source (CV-LS)	LED light source
(D)	Thorlabs DDSM100	Direct-drive linear translation stage, providing 100 mm of travel with 500 nm resolution
(E)	Thorlabs KBD101	and a maximum speed of 500 mm/s
(F)	Teledyne Dalsa Xtium-CL MX4	Direct-drive brushless linear servo motor
(G) and (H)	Thorlabs LNR25ZFS with ZFS25B	Frame grabber card that supports the line scan camera
(I)	Thorlabs KST101	Linear translation stage fitted with a compact stepper motor actuator
(J)	Thorlabs PY004	Compact single channel controller stepper motor
(K)	Thorlabs MLJ150	High load pitch yaw platform

10 min for the matrix to relax. From the step displacement to the duration of the hold time, the entire sample gauge length is automatically scanned with the high-resolution line scan camera (A) to locate all fiber breaks. The key design mechanism of the system is the horizontal motor (D) that drives the line scan camera across the entire gauge length of the specimen. The translation stage is driven by a direct-drive brushless linear servo motor and a 500 nm resolution linear optical encoder with controller (E). The stage (D) is electrically integrated with the camera via a frame grabber card (F), such that each line of the image is 500 nm from the previous line, and ± 1.5 µm from the same line on the previous image. The motor (D) provides acceleration (up to 500 mm/s^2) and velocity (up to 3000 mm/s), both of which far exceed the 50 kHz triggering limits of the camera (A).

This optical system is mounted on four axes of motion in addition to the (D) stage: vertical, depth (to focus), tilt, and yaw. These provide fine positioning of the objective, so that the entire gauge length of the embedded fiber remains in focus and in frame during the test. The (D) stage is mounted on a linear translation stage (G) fitted with a compact stepper motor actuator (H) with a theoretical step size of 0.46 nm. The stepper motor (I) allows for continuously variable speeds, and the actuator (H) uses integrated hard stops to automatically cut the power when the motor reaches its mechanical limits. Beneath the stage (G) is a high load pitch yaw platform (J) which is mounted 90° from the direction of the camera such that the pitch axis provides fine alignment of the direction of travel of the (D) stage with the fiber, while the yaw axis keeps the fiber in focus over the entire range of travel. Supporting this is a stepper motor lab jack (K) with a 20 kg load capacity and 10 µm unidirectional positioning, repeatability allowing the entire apparatus to be rapidly moved (3 mm/s) to bring a fiber into the center of the frame. The entire apparatus is mounted on an optical vibration isolation table.

Tensile Frame

This motion-controlled camera system is placed in front of an ADMET eXpert 4100 MicroTester (Fig. 1) with a 1 kN load cell, 25 mm stroke, and 10 nm position resolution. The MicroTester was customized with a cutout behind the sample area, attached to the guided slide (Fig. 1 and Fig. S4 in the S.M.), to allow light transmission and a linear translation platform to increase linearity of motion and prevent the specimen from moving out of focus during the experiment.

Grips were machined to put the center axis of ASTM D638-14 type IV dogbones [31] with up to 2 mm thickness along the center of the crossheads, while allowing the camera and light source to come within 1 cm of the surface of the specimen. Figure 1 shows the complete apparatus for straining single fiber composite specimens, and the inset shows a closeup image of a single fiber composite with two visible fragments acquired by the camera post-straining.

Operation of the System

The system acquires images while the linescan camera travels along the gauge length of the specimen (Fig. 2(a)). The camera motion control software (Thorlabs Kinesis) is programmed with a unified "sequence," producing a reproducible camera protocol file containing accessible tuning parameters for focus, alignment, and image acquisition. Live controller status information is displayed and output to a log file useful for correlating camera motions to data produced by the load frame and camera.

The load frame control software (ADMET MTEST-Quattro) has a similar capability to automate and execute a step-strain sequence on the specimen, in accordance with the DiBenedetto-Drzal test protocol, while

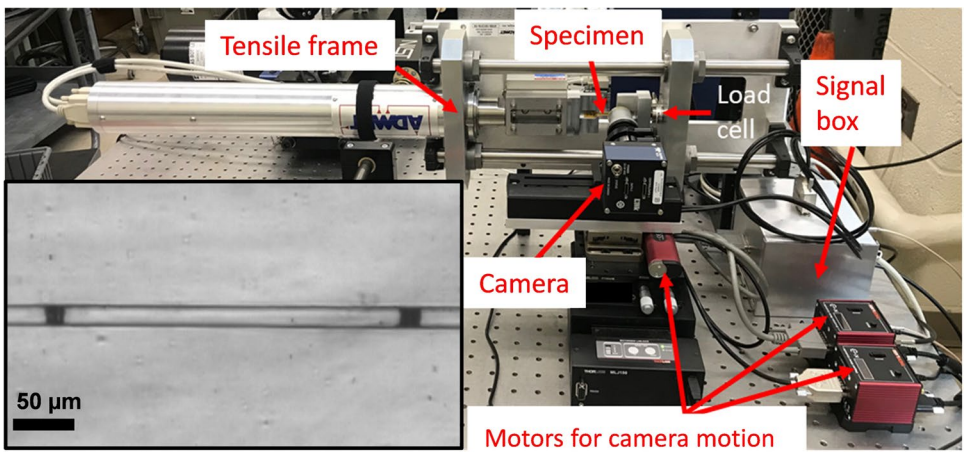

Fig. 1 Automated fiber fragmentation testing apparatus named "Snappy;" inset of a closeup image of a single fiber composite with two visible breaks acquired by the camera

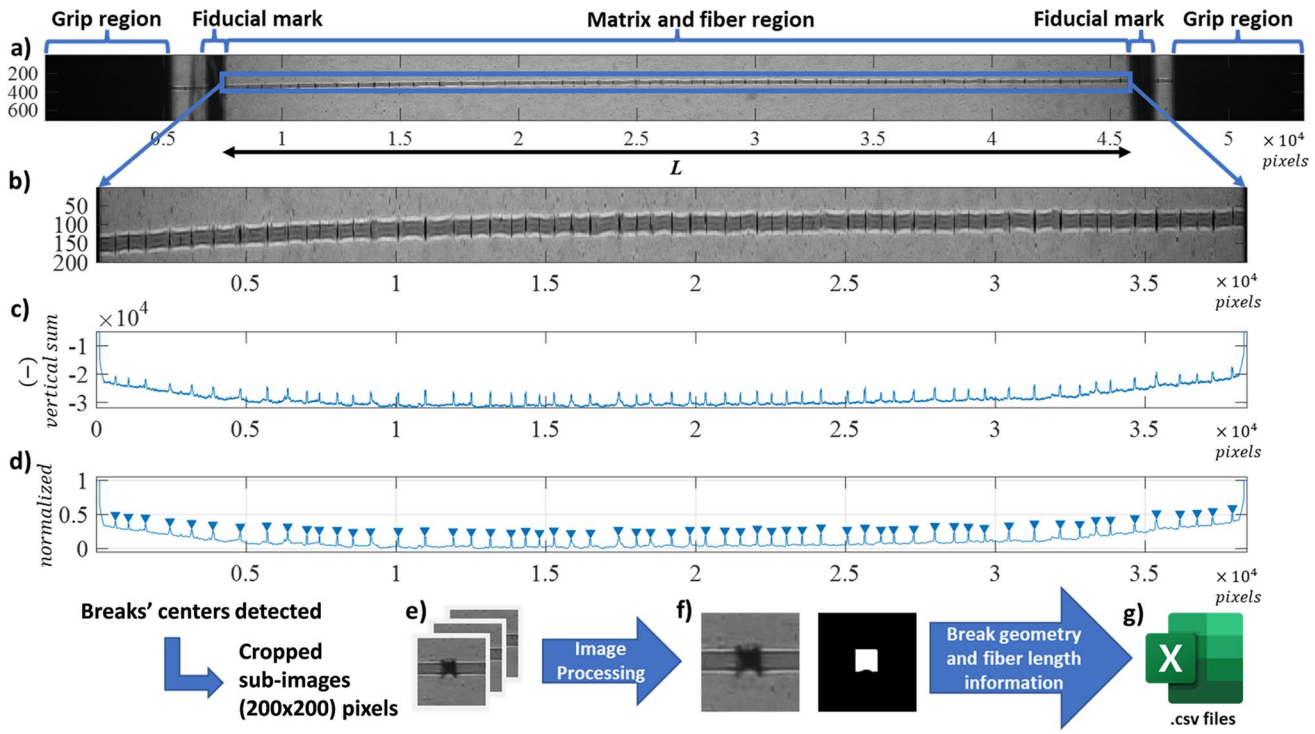

Fig. 2 Image analyses workflow. **a**) An example of the image quality captured by the optical system; for illustration purposes, the unstressed image at the end of the test that includes all fiber breaks is shown; **b**) cropped unstressed image with fiber breaks spatially numbered from left to right; **c**) negative of the pixel sum vector (i.e., grayscale pixel values are summed in the vertical direction); **d**) peaks of the negative sum vector represent the breaks between the fiber fragments; **e**) sub-images for each break (automatically cropped by using the break center locations obtained from the peaks above; **f**) before and after image processing applied on a sub-image; **g**) break geometry; and fiber length information stored in a.csv spreadsheet

displaying and recording force and crosshead displacement as a function of time.

A custom image data acquisition program based on the linescan camera low-level application programming interface (API) (Teledyne Dalsa Sapera Basic C API) was written to read the configuration files of (A) and (F) (in Table 1) and efficiently write the acquired images to disk as tagged image file format or .TIFF files named according to the time of acquisition, along with a text-based display of important instrument status information and a graphical display of the most recently acquired image. These stored .TIFF images are subsequently analyzed in an offline digital image analysis workflow to be described later.

This multi-program control system is possible because the controller (E) generates voltage outputs that we use to electrically, rather than programmatically, control the direction mode and the line trigger of the sensor (A), and frame trigger of (F) (in Table 1). The user then needs only to prepare a motion sequence and strain sequence while the load frame is in standby mode, then activate the motion sequence before activating the strain sequence.

Automated Single Fiber Fragmentation Test

Snappy's design and operation have been described above. Image calibration is first performed at the time of the test to quantify measurement uncertainty in the entire field of view prior to loading the specimen in the test area, as shown in Fig. 3. For the calibration and tests conducted in this paper, a velocity of 16 mm/s and acceleration of 200 mm/s^2 were chosen, resulting in an image acquisition time of 2.5 s for a 26.5 mm of travel (grip-to-grip).

The calibration method consists of using a dual axis linear scale micrometer glass slide, also known as a reticle, that is approximately 76.20 mm (±0.10 mm) in length and 25.40 mm (±0.10 mm) in width. The graduations on the scale extend to 25 mm in the horizontal axis and 15 mm in the vertical axis, with divisions of 25 µm (see Fig. 4).

The slide is positioned vertically to fit between the grips of the test section. The horizontal traversal of the camera system captures images of the micro stage tool's linear and vertical axes. Based on the reticle shown in Fig. 4, and the 16 mm/s velocity of the camera, the pixel size was determined to be

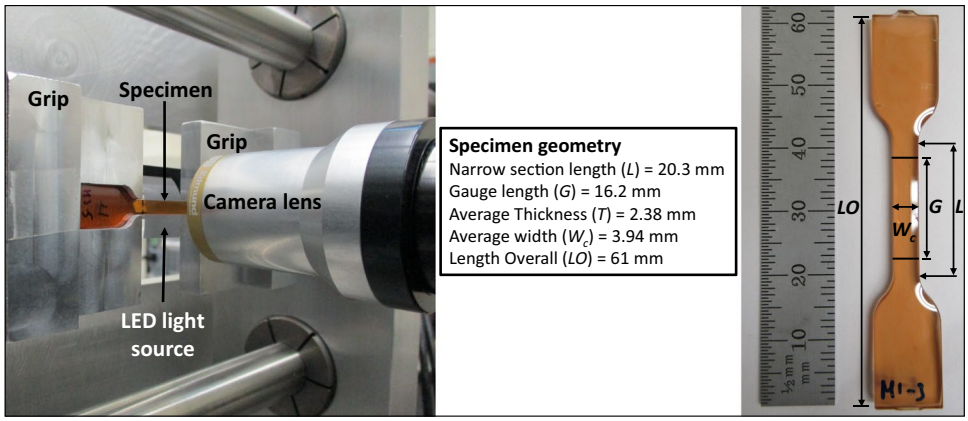

Fig. 3 Specimen loaded in the test section of the tensile frame. During a typical tensile experiment, the LED light source located behind the specimen test section is turned on, and the camera scans the narrow section of the specimen

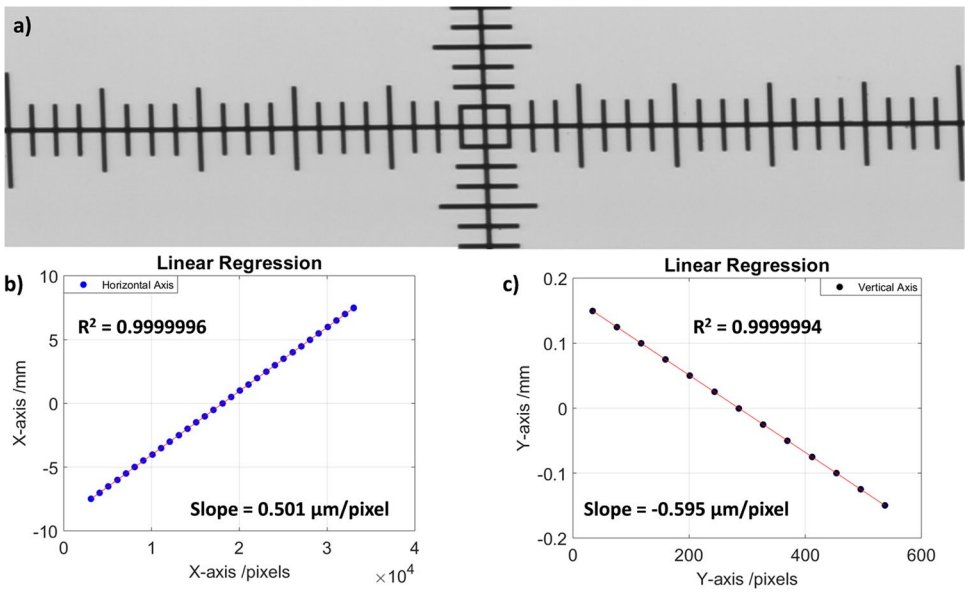

Fig. 4 (**a**) 2D image of the reticle for the optical microscope calibration scale. Each division is 25 µm in the horizontal and vertical directions. A linear regression model was used to fit the data of (**b**) the horizontal and (**c**) the vertical axes, and the R-squared numbers for each fit are 0.9999996 and 0.9999994, respectively

0.595 µm in the vertical direction and 0.501 µm in the horizontal direction. Thus, the size of each line image with the 21.17X magnification is 1126.4 µm × 1.0 µm. At an acquisition rate of 50 kHz and camera travel velocity of 16 mm/s, this results in 3.125-line images being acquired every 1 µm in the horizontal direction. Coupled with the summing algorithm within the camera system, the image size for the 26.5 mm travel distance is 53000 pixels × 2048 pixels. The 2D image (Fig. 2(a)) was cropped in the vertical direction to 53,000 pixels × 550 pixels, yielding a field of view (FOV) of 26,500 µm x 302.5 µm, which is the region of space projected through the lens system onto the camera detector. This FOV size can be adjusted horizontally by selecting (from Table 1) the (D) motion start and stop positions and vertically cropping the image in the camera software, which is done prior to the start of the test.

For the automated SFFT, the loading is done in a series of small displacement steps programmed in ADMET-MTEST-Quattro software. The test settings used here are 31 strain-steps with a nominal strain increase of 0.003 mm/mm (i.e.: 0.08601 mm ± 0.00006 mm crosshead displacement increase) and a 10-min delay between each strain-step. The total crosshead displacement (in loading) is 2.66653 mm ± 0.00007 mm (as illustrated in Fig. S5a of the S.M. document).

Figure 5 shows that as the strain increases, the relaxation behavior of the matrix becomes more pronounced. This is consistent with the constitutive law governing the behavior of linear viscoelastic materials to step-strain and responses, which was previously discussed in [32]; however, the onset of fiber fracture occurs in the nonlinear relaxation region. This means that there is a need for a nonlinear viscoelastic shear lag model to accurately capture the change in the matrix modulus with each strain step. Image acquisition for this experiment was acquired with a 38 s interval. A total of three specimens were tested, and for each experiment, more than 500 images were acquired during the loading and unloading of the test. Figure 5 also shows the load-time curve with each new break (open black squares) that appeared during image acquisition (solid red dots). After each strain increment, the

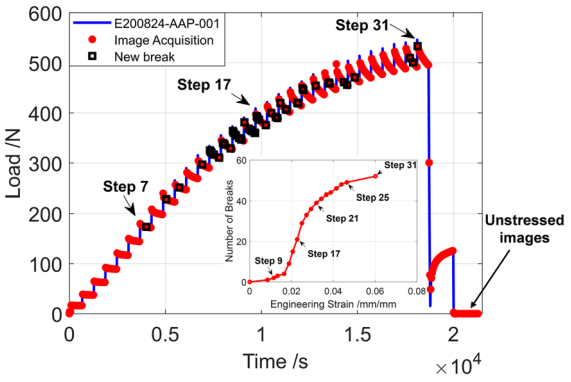

Fig. 5 Load versus time with fiber break evolution. Image acquisition is shown in solid red dots on the load versus time curve with images acquired every 38 s. Fiber breaks are illustrated as open black squares. Unstressed images are acquired at the end of the test. The inset image shows a line plot of the fiber break evolution as a function of engineering strain taken from fiducial marks on images

matrix is allowed to relax for 10 min. During that period of relaxation, the load visibly decreases.

In Fig. 5, at low step-strain (first region) between steps 7 to 12, few fiber breaks occur. Then, a cascade of breaks occurs between steps 13 to 19 (second region); in addition, the matrix is undergoing significant relaxation. As the strain increases, the matrix exhibits more pronounced viscoelastic behavior. Finally, from step 20 to the end (step 31), the fiber break occurrence slows down (third region). The inset image in Fig. 5 shows the fiber break evolution as a function of engineering strain, and the cascade of fiber breaks (steps 13 through 19) is seen as a rapid increase in slope between 0.019 mm/mm to 0.029 mm/mm strain. As the curve begins to plateau (steps 21 to 31), the loading segment of the SFFT approaches saturation, and the fiber break occurrence decreases significantly. However, step 31 shows that saturation was not achieved, which is defined by Drzal and DiBenedetto as the occurrence of 3 to 5 strain steps in which no additional break occurs.

On Fig. 2(b), the break locations are typically numbered spatially from left to right on the unstressed image after acquired images are processed. Each break occurrence during the test is catalogued with respect to strain, step, and time in the following figure collage (Fig. 6) of matrix relaxation periods.

Figure 6 shows multiple relaxation period scans between each 10-min time interval (i.e., step). It is a closeup examination of each relaxation period of Fig. 5. Each scan shows image acquisition (in solid red dots) and each newly occurred fiber break (in solid black squares) observed during image acquisition within a step. If a step is skipped in Fig. 6, it means that no fiber break occurred during that 10-min interval. The 10-min dwell time used by Drzal [5] seems to be reasonable, since a quiescent period of more than 30 s (except for Fig. 6(h)) is established where no fiber breaks occur prior to the initiation of the next strain step. Thus, the rapid scanning feature implemented in Snappy supports the DiBenedetto-Drzal test protocol and underscores that any acceleration of the typical 6 h test time for the SFFT by decreasing the 10-min dwell time is known to lead to a different IFSS value when tier 3 data is analyzed.

Based on the research of Li et al. [23], this indicates that the most promising approach for increasing the data output from this test is to use multi-fiber fragmentation test (MFFT) specimens. Specifically, the fibers in the MFFT specimen must be spaced far enough apart, so they do not interact, thereby, creating multiple individual single fiber regions. For example, the rapid image acquisition feature of Snappy, along with its ability to scan multiple regions within a dog-bone specimen can effectively reduce the testing time for a 3-fiber MFFT test specimen to 2 h from 6 h for a SFFT.

Automated Algorithm for Extracting Tier 1 Data from Snappy Images

A typical image for the automated feature extraction is shown in Fig. 2(a). The two main features that must be extracted from this image are the fiducial mark locations and the fiber break locations.

Extraction of Fiducial Mark Data for Fiber Strain Determination

The automated fiducial mark data extraction feature developed in this work allows the fast tracking and calculation of strain data (associated with each fiber break), which was done manually on the original automated SFFT system [25]. This new feature reduces the processing time from days to seconds. The area of interest is cropped from the middle portion (highlighted in Fig. 2(b)) by detecting the edges where the fiducial marks and the middle region meet. This is accomplished by considering the sum of the pixel intensities in the image in the vertical direction. Because of the high contrast between the fiducial marks (dark) and the sample region (light), the edge of the fiducial mark region was accurately identified from the summed values in an automated protocol. Since every pixel of the continuous dark regions in the image (e.g., fiducial marks and grip regions) has very similar intensity values, these regions emerge as plateaus in the vertical summation data. To determine the starting and ending points of these plateaus, which is used to crop the sample region, the change of every consecutive point of the summation data (i.e., derivative) is calculated where the plateaus have minimum change (i.e., derivative is zero or almost zero). After finding the ending point of the left fiducial mark and beginning point of the right fiducial mark (i.e., the points with minimum

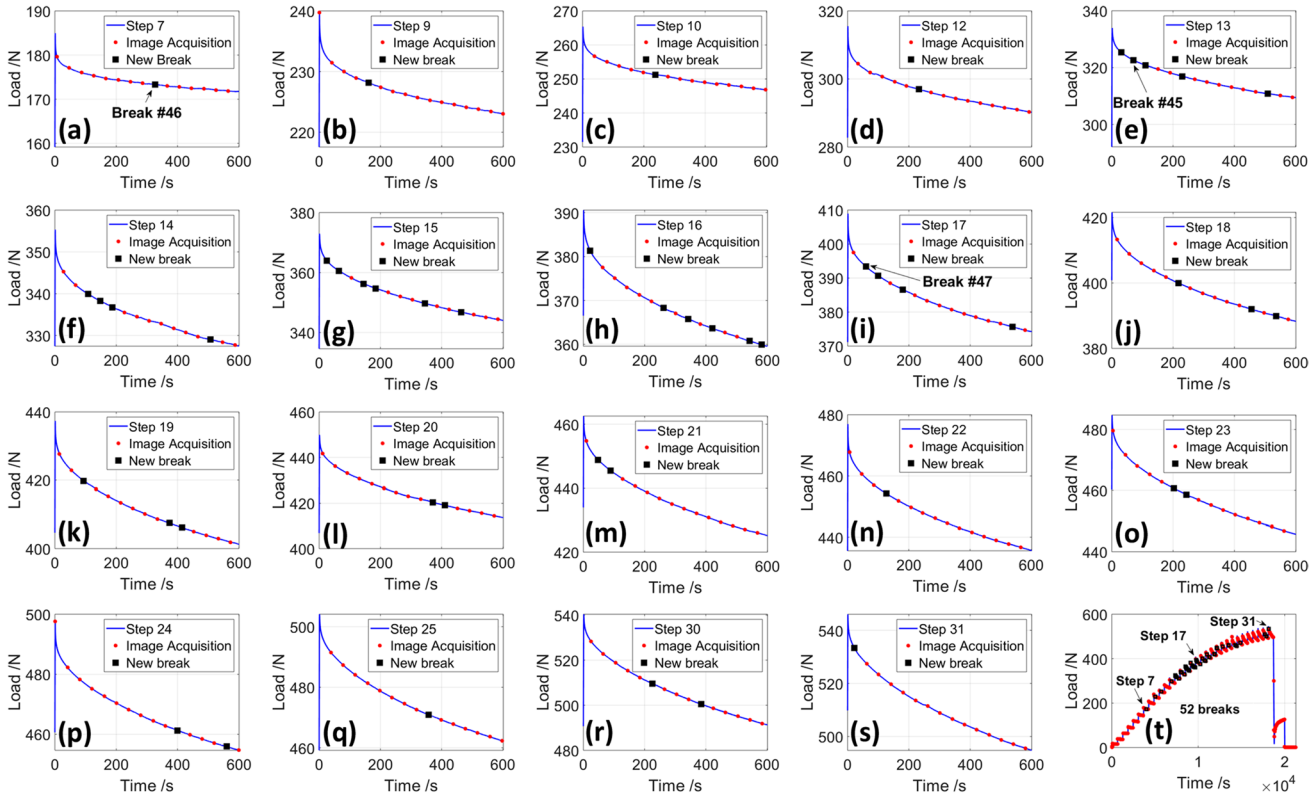

Fig. 6 (**a**)-(**s**) Load versus time scans of the SFFT 10-min relaxation period. Image acquisition (solid red dots) and newly observed fiber breaks (in solid black square) are shown. The fiber break numbers are based on the numbering shown in 4b (spatially from left to right) on the unstressed image acquired at the end of the test

derivative values which are closest to the middle point), the sample region is cropped from the points. Furthermore, the distinct gauge length region looked the same on all the images, making it easy to crop. The length of these cropped images increased as the sample was subjected to tensile loading. This cropped image length information is recorded and used to calculate the engineering strain.

The negative of the summed values in the vertical direction in the matrix and fiber region is plotted in Fig. 2(c), which clearly identifies the horizontal locations of fiber breaks as peaks (see Fig. 2(d)). The global engineering strain is calculated by the change in the gauge length, L, defined by the fiducial marks in Fig. 2(a), to the original length, L_0, (equation (1)). The engineering strain versus time plot is shown in Fig. S6 of the supplementary material.

$$\varepsilon = \frac{L}{L_0} - 1 \tag{1}$$

Extraction of Fiber Break Location Data

The fiber break locations were extracted from each image by performing a series of digital image analysis protocols. All images were analyzed using the same workflow. Each image covered a rectangular area consisting of fiber and matrix regions in the middle and the grip regions at both ends (Fig. 2(a)). Since there is no interest in the grip regions, the area of interest is cropped from the middle portion by detecting the edges where the grip and the middle regions meet, as described earlier in Fig. 2(b). The negative of the summed values in the vertical direction in the matrix and fiber region is plotted in Fig. 2(c), which clearly identifies the horizontal locations of fiber breaks as peaks (Fig. 2(d)). A similar strategy of summed values in the horizontal direction was used to identify the vertical location of the fiber breaks. The horizontal and vertical locations of the fiber breaks are then used to crop a small sub-image of size 200 pixels × 200 pixels (100 μm × 100 μm) around each fiber break location (Fig. 2(e)). Each sub-image is then further analyzed for precise fiber break locations.

The four corner locations of the fiber break region are identified in each sub-image in an automated protocol. This is accomplished using a sequence of image processing algorithms that included operations such as sharpening, noise removal (smoothing), image segmentation, erosion, and dilation. Similar operations have been used extensively in material science research to detect

different features of interest in micrographs of material microstructures [33–35]. The protocol developed specifically for the present problem started with noise removal, which smooths the images by modifying undesirable pixel values (i.e., darker pixels in the matrix region). Since it is very important to preserve the edges corresponding to the fiber break in the image, an edge-preserving median filter was preferred [36], and MATrix LABoratory or MATLAB's '*medfilt2*' function was used to filter the sub-images [37]. After de-noising, a sharpening algorithm was employed to make the edges more distinct, i.e., MATLAB's '*imsharpen*' function was used, so that the fiber break region became clearly discerned in each sub-image [37]. Furthermore, a segmentation algorithm called adaptive thresholding was used to label the pixels in the de-noised and sharpened grayscale image as either 0's (matrix) or 1's (break) [38]. The resultant binary image (obtained after thresholding) was cleaned-up by morphological operations such as erosion and dilation. The finalized binary image (Fig. 2(f)) was then ready for precise marking of the four corners of the break region. This task was accomplished by fitting a bounding rectangular box to the segmented fiber break region using the '*regionprops*' function in MATLAB [37]. The X and Y coordinates of the four corners are automatically stored in a spreadsheet or a comma-separated value (.csv) file (Fig. 2(g)). Using two consecutive locations of the fiber break regions, the fiber break length is calculated and saved in the same.csv file.

The image analysis protocols described above are computationally efficient and greatly reduces the data analysis time to address a further disadvantage of manual methods listed in Table S1 (in the S.M. document). As a test of the algorithm's ability to accurately detect each fiber break, automated break location data was compared to manual data (Fig. 7). The four corners and the centroid for each break are detected. Manual fiber break locations are plotted in blue dots and automatically detected locations in red dots.

Figure 8 shows three images of a segment of a single fiber composite specimen at different times during testing. Figure 8(a) and (b) are images acquired subsequently during the same loading step #30 while maintaining a constant strain, hence, the global strain remaining constant (0.060 mm/mm). However, after unloading the specimen (unstressed length) in Fig. 8(c), the global strain decreases significantly (0.016 mm/mm).

The fiber strain depends on each fiber fragment, which can be automatically determined from the fiber break location tracking. Each fiber fragment length can be referenced to the unloaded specimen fragment length, shown in Fig. 8(c), which contains all the breaks at an "unstressed" length. The fast acquisition rate of Snappy and the automated fiber break location tracking provide the possibility for determining the fiber strain, which is a step toward calculating the strength in the fiber at the critical length, and subsequently the IFSS.

The image in Fig. 8(c) appears blurry because it was not refocused at the end of the test. Some user input may be needed (at the end of the SFFT) to refocus the last image acquired after the unloading event to extract accurate estimates of the strength of the fiber at the critical length, l_c, and additional features necessary for applying the appropriate shear lag models

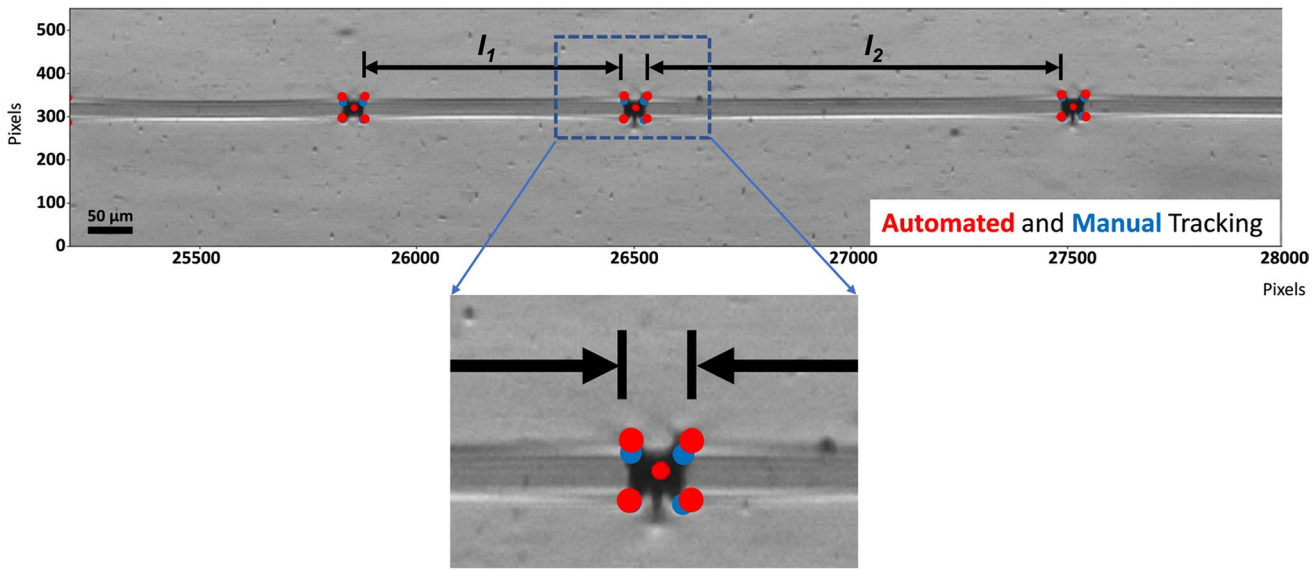

Fig. 7 Manually identified fiber break locations (blue dots). Fiber break four corners and centroid data are automatically detected and plotted in red on an image acquired during the SFFT. The fragment lengths (e.g., l_1 and l_2, which are distances between each break) are determined automatically on each image and stored in the comma-separated value (.csv) spreadsheet

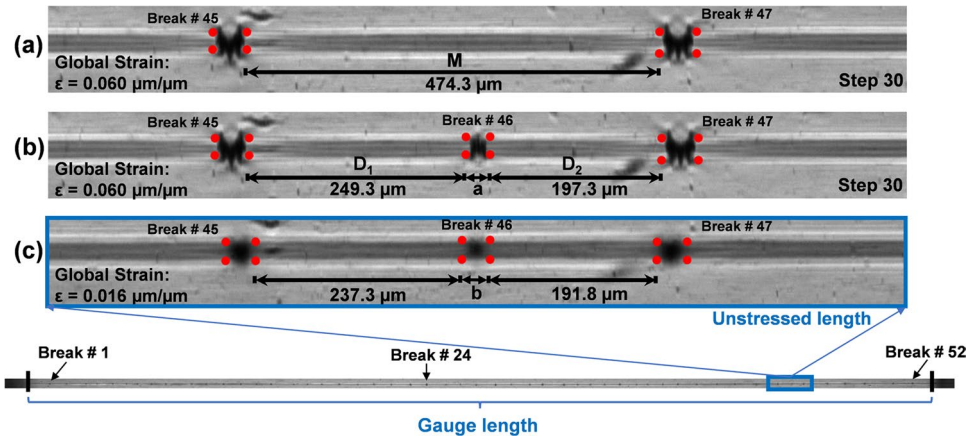

Fig. 8 Single fiber composite specimen. Image (**a**) represents a segment of the single fiber composite under load (502 N and 0.060 mm/mm strain) during the loading part of the SFFT. The embedded fiber shows two breaks and their highlighted locations. Image (**b**) was acquired right after (a) during the same step (#30) and shows that a new break occurred; de-bonded length a = 25.5 μm. Image (**c**) represents the same segment with the fiber break locations after unloading the specimen (unstressed image) and de-bonded length b = 25.5 μm

to calculate IFSS values. This effort will be the subject of future work.

Conclusion

Snappy was designed to improve on earlier attempts at automating the single fiber fragmentation test (SFFT), which measures the interfacial shear strength (IFSS) in fiber reinforced composite materials. Snappy provides great advances in data acquisition and processing needed to extract features necessary to determine the strength of the fiber at the critical length, l_c, which is subsequently applied to shear lag models to calculate IFSS values. The following highlights Snappy's advances:

- The rapid image acquisition feature implemented in Snappy allows the complete examination of the fiber break evolution process within each strain step.
- Data presented in this paper supports the need for the at least 10-min test protocol implemented by DiBenedetto and Drzal to accommodate time-dependent fracture of the fiber due to the viscoelastic nature of the matrix in the single fiber composite.
- The automated image acquisition feature, coupled with the ability of the new instrument to scan multiple regions within each dogbone, offers the promise of accelerating the data output of this test by using multifiber fragmentation test (MFFT) specimens where the fibers are well spaced.
- The automated fiber detection algorithm implemented in this new instrument allows for the rapid acquisition of tier 1 data. These automated features should reduce the tediousness of this test, facilitate the standardization of this testing protocol, and allow for the rapid implementation of this automated test throughout industry.

Future research at NIST will focus next on demonstrating how to calculate the strength of the fiber at the critical length from saturated tier 1 data. Additionally, a more rigorous examination of the statistics of the fiber fragmentation process, particularly, the testing of closely spaced multifiber arrays should help quantify the fiber–fiber interaction effect that occurs in real composites.

Supplementary Information The online version contains supplementary material available at https://doi.org/10.1007/s40799-022-00611-3.

Acknowledgements The authors would like to thank Christopher Amigo for providing manufacturing support. We would like to also thank Christopher Soles for helpful suggestions and comments regarding this study. The authors Sezen Yucel, Berkay Yucel, and Surya Kalidindi acknowledge support from the USDA Forest Service award GR10004954 and ONR award N00014-18-1-2879.

Declarations

Declaration of interests The authors declare that they have no known competing financial interests or personal relationships that could have appeared to influence the work reported in this paper.

Disclaimer Certain commercial equipment, instruments, or materials are identified in this paper in order to specify the experimental procedure adequately. Such identification is not intended to imply recommendation or endorsement by the National Institute of Standards and Technology, nor is it intended to imply that the materials or equipment identified are necessarily the best available for the purpose.

References

1. Civil Engineering Research Foundation (2001) Gap analysis for durability of fiber reinforced polymer composites in civil infrastructure. The Civil Engineering Research Foundation, Washington, DC

2. Hunston DL, Bascom WD, Wells EE et al (1980) Viscoelastic characterization of structural adhesive via force oscillation experiments. In: Lee L-H (ed) Adhesion and Adsorption of Polymers. Springer, US, Boston, MA, pp 321–339
3. Globalization of Materials R&D (2005) Time for a national strategy. Committee on globalization of materials research and development, National Research Council, Washington, p 216. http://www.nap.edu/catalog/11395.html
4. Pitkethly MJ, Favre JP, Gaur U et al (1993) A round-robin programme on interfacial test methods. Compos Sci Technol 48:205–214. https://doi.org/10.1016/0266-3538(93)90138-7
5. Rich MJ, Drzal LT, Hunston DL, Holmes, GA, McDonough, WG (2002) Round robin assessment of the single fiber fragmentation test. In: Proceedings of the 17th Technical Conference of the American Society for Composites. Am Soc Compos pp 1–9. https://tsapps.nist.gov/publication/get_pdf.cfm?pub_id=860441
6. Lodeiro, MJ (2001) Investigation of PMC interface properties using the single-fibre fragmentation technique. NPL Report. MATC(A)16. https://eprintspublications.npl.co.uk/2010/1/MATC16.pdf
7. Curtin WA (1991) Exact theory of fibre fragmentation in a single-filament composite. J Mater Sci 26:5239–5253. https://doi.org/10.1007/BF01143218
8. Fraser WA, Ancker FH, Dibenedetto AT (1975) A computer modelled single filament technique for measuring coupling and sizing agent effects in fibre reinforced composites. In: Proceedings of the 30th Annual Technical Conference on Reinforced Plastics. The Society of Plastics Industry. Section 22–A
9. Drzal LT, Rich MJ, Camping JD, Park WJ (1980). Interfacial shear strength and failure mechanisms in graphite fiber composites. In: Proceedings of the 35th Annual Technical Conference, Reinforced Plastics/Composites Institute of the Society of the Plastics Industry, Inc. Sec 20-C, New Orleans, pp 1–7. http://pascal-francis.inist.fr/vibad/index.php?action=getRecordDetail&idt=PASCAL8130158357
10. Fraser WA, Ancker FH, Dibenedetto AT, Elbirli B (1983) Evaluation of surface treatments for fibers in composite materials. Polym Compos 4:238–248. https://doi.org/10.1002/pc.750040409
11. Netravali AN, Topoleski LTT, Sachse WH, Phoenix SL (1989) An acoustic emission technique for measuring fiber fragment length distributions in the single-fiber- composite test. Compos Sci Technol 35:13–29. https://doi.org/10.1016/0266-3538(89)90068-7
12. Johnson W, Lagace P, Masters J et al (1991) On the determination of fiber strengths by in-situ fiber strength testing. J Compos Technol Res 13:22. https://doi.org/10.1520/CTR10070J
13. Netravali AN, Sachse W (1991) Some remarks on acoustic emission measurements and the single-fiber-composite test. Polym Compos 12:370–373. https://doi.org/10.1002/pc.750120510
14. Netravali AN, Li Z-F, Sachse W, Wu HF (1991) Determination of fibre/matrix interfacial shear strength by an acoustic emission technique. J Mater Sci 26:6631–6638. https://doi.org/10.1007/BF02402656
15. Sachse W, Netravali AN, Baker AR (1992) An enhanced, acoustic emission-based, single-fiber-composite test. J Nondestruct Eval 11:251–261. https://doi.org/10.1007/BF00566415
16. Feillard P, Désarmot G, Favre JP (1993) A critical assessment of the fragmentation test for glass/epoxy systems. Compos Sci Technol 49:109–119. https://doi.org/10.1016/0266-3538(93)90050-Q
17. Feillard P, Rouby D, Désarmot G, Favre JP (1994) Limits of conventional micromechanical analysis of interface properties in glass-epoxy model composites. Mater Sci Eng A 188:159–166. https://doi.org/10.1016/0921-5093(94)90368-9
18. Manor A, Clough RB (1992) In-situ determination of fiber strength and segment length in composites by means of acoustic emission. Compos Sci Technol 45:73–81. https://doi.org/10.1016/0266-3538(92)90124-L
19. Rouby D, Favre JP (1986) Study of fiber failures in a single carbon fiber-epoxy matrix composite by using acoustic emission. In: Proceedings of the 16th Annual Meeting of the European Working Group on Acoustic Emission (EWGAE), London
20. Clough R (1996) The measurement of fiber strength parameters in fragmentation tests by using acoustic emission. Compos Sci Technol 56:1119–1127. https://doi.org/10.1016/S0266-3538(96)00076-0
21. Kim J, Leigh S, Holmes G (2009) E-glass/DGEBA/ *m* -PDA single fiber composites: new insights into the statistics of fiber fragmentation: E-Glass/DGEBA/ *m* -PDA single-fiber composites. J Polym Sci Part B Polym Phys 47:2301–2312. https://doi.org/10.1002/polb.21818
22. Holmes GA, Wesson S, McDonough WG et al (2009) An automated testing machine for monitoring the evolution of fiber breaks. J Mater Sci 44:2007–2015. https://doi.org/10.1007/s10853-009-3294-1
23. Li Z-F, Grubb DT, Phoenix SL (1995) Fiber interactions in the multi-fiber composite fragmentation test. Compos Sci Technol 54:251–266. https://doi.org/10.1016/0266-3538(95)00056-9
24. Holmes GA, Kim JH, Leigh S, McDonough W (2010) The single fiber composite test: A comparison of E-glass fiber fragmentation data with statistical theories. J Appl Polym Sci NA-NA. https://doi.org/10.1002/app.31002
25. Holmes GA, Peterson RC, Hunston DL, McDonough, WG, Schutte, CL (2000) The effect of nonlinear viscoelasticity on interfacial shear strength measurements. In: Schapery RA, Sun CT (eds) Time Dependent and Nonlinear Effects in Polymers and Composites. ASTM International, West Conshohocken, pp 98–117. https://doi.org/10.1520/STP15831S
26. Kim JH, Hettenhouser JW, Moon CK, Holmes GA (2009) A fiber placement device and methodology for preparing 2-D and 3-D combinatorial microcomposites. J Mater Sci 44:3626–3632. https://doi.org/10.1007/s10853-009-3362-6
27. Wagner HD, Steenbakkers LW (1989) Microdamage analysis of fibrous composite monolayers under tensile stress. J Mater Sci 24:3956–3975. https://doi.org/10.1007/BF01168959
28. McCarthy ED, Kim JH, Heckert NA et al (2015) The fiber break evolution process in a 2-D epoxy/glass multi-fiber array. Compos Sci Technol 121:73–81. https://doi.org/10.1016/j.compscitech.2014.10.013
29. Woodcock JW, Sheridan RJ, Beams R et al (2020) Damage sensing using a mechanophore crosslinked epoxy resin in single-fiber composites. Compos Sci Technol 192:108074. https://doi.org/10.1016/j.compscitech.2020.108074
30. Holmes GA, McDonough WG (2002) E-Glass/DGEBA/m-PDA model composites: time dependent failure in a brittle multi-fiber composite. In the Proceedings of the 47th International SAMPE Symposium and Exhibition, Volume 47, Issue 2/2, pp 1690–1702. https://tsapps.nist.gov/publication/get_pdf.cfm?pub_id=851988
31. D20 Committee (2017) Test method for tensile properties of plastics. ASTM International. https://doi.org/10.1520/D0638-14
32. Hunston D, Holmes G, Peterson R (1999) Viscoelastic properties of a resin commonly used in the single fiber fragmentation test. J Reinf Plast Compos 18:1646–1657. https://doi.org/10.1177/073168449901801801

33. Iskakov A, Kalidindi SR (2020) A framework for the systematic design of segmentation workflows. Integr Mater Manuf Innov 9:70–88. https://doi.org/10.1007/s40192-019-00166-z
34. Yucel B, Yucel S, Ray A et al (2020) Mining the correlations between optical micrographs and mechanical properties of cold-rolled HSLA steels using machine learning approaches. Integr Mater Manuf Innov 9:240–256. https://doi.org/10.1007/s40192-020-00183-3
35. Yucel S, Moon RJ, Johnston LJ et al (2021) Semi-automatic image analysis of particle morphology of cellulose nanocrystals. Cellulose 28:2183–2201. https://doi.org/10.1007/s10570-020-03668-8
36. Jain R, Kasturi R, Schunck BG (1995) Machine vision. McGraw-Hill, New York
37. MATLAB (2019) MATLAB and image processing toolbox release notes R2019b, The MathWorks, Inc., Natick, Massachusetts. https://www.mathworks.com/help/images/release-notes.html
38. Davies ER (2005) Machine vision theory, algorithms, practicalities. Morgan Kaufmann, Amsterdam, Oxford